Koc. J. Sci. Eng., 6(2): (2023) 162-171 https://doi.org/10.34088/kojose.1233583

Kocaeli University

Kocaeli Journal of Science and Engineering

http://dergipark.org.tr/kojose

Transcutaneous Nerve Stimulation Current Thresholds Based on Nerve Bending Angle and Nerve Termination Point

Enver SALKIM [1, 2, *]

[1] *Department of Electronics and Automation, Muş Alparslan University, Muş, Turkey,* ***ORCID:*** *0000-0002-7342-8126*
[2] *Department of Electronics and Electrical Engineering, University College London (UCL), London, UK*

Article Info

Research paper

Received : *January 13, 2023*
Accepted : *May 4, 2023*

Keywords

Electrical Stimulation
FEM Computational Models
Nerve Bending
Nerve Termination
Neuromodulation Therapy

Abstract

There is increasing interest in using transcutaneous electrical stimulation to treat or suppress brain-related disorders. Primary headache disorder is a socioeconomic burden whose pharmaceutical and invasive treatment method may have troublesome side effects. There are various transcutaneous electrical nerve stimulation neuromodulation systems that are used for health-related disorders. TMany factors may affect these systems' efficiency, including stimulus current levels. A device for primary headaches showed mixed results. This may be related to the higher stimulus current levels that are applied through the electrodes. A feasible solution to reduce the required current levels is considering the geometrical features of the target nerve bending and nerve termination trajectories. In this study, the impact of the geometrical features of the nerve, such as nerve bending and nerve termination, on the stimulus current thresholds were analyzed based on FEM hybrid models. Twenty nerve models were generated considering statistical variations to assess the effect of the nerve geometrical features on the target neuromodulatory system. Finally, the safety parameters were calculated based on the target neuromodulator settings. The results showed that the geometric features of the target nerve have a significant effect on the required stimulus current thresholds. These results may provide important guidance mainly for transcutaneous nerve stimulation and future electrical nerve stimulation design.

1. Introduction

Transcutaneous electrical nerve stimulation (TENS) is a non-invasive method that is used globally to restore the function of biological disorders. In this technique, the current is applied through the skin via surface electrodes to depolarize the neural tissue underneath. Application of the extracellular stimulation of the peripheral nerve can restore the function of these neurological diseases or injuries by means of generation, inhibition, and modulation of brain activity [1]. The use of TENS as a therapy technique to treat primary headache disorders is growing. The primary headache disorders may be grouped as migraine, cluster headache, and tension-type headache, the most common diseases and leading causes of disability worldwide [2]. Migraine is a disabling neurological disorder (11.6%) [3] characterized by recurrent attacks of moderate to severe head pain associated with nausea, vomiting, photophobia, and phonophobia [2]. Transcutaneous frontal nerve stimulation (t-FNS) is a peripheral neuromodulation method that has shown some positive results in migraine treatment. This promising non-invasive neurostimulatory therapy with Cefaly (Cefaly, CEFALY Technology, Lige, Belgium) stimulator has been developed to prevent an episodic migraine by stimulating the supraorbital (SON) and supratrochlear (STN) nerves which are the branches of frontal nerve [4]. This neuromodulator generates electrical pulses and transmits them via an electrode to the forehead area to activate the SON and STN nerve branches for alleviating pain, as shown in Figure 1. Studies on the effectiveness of the neuromodulator have shown mixed results [5, 6]. These complications can be associated with the required high current levels [7], due to the variations of the neuroanatomical structures.

It has been shown that the stimulus current levels of the nerve fibers may vary based on the geometric features

* Corresponding Author: e.salkim@alparslan.edu.tr

of the nerve trajectory, including nerve bending and nerve termination [8, 9]. These conditions may also have an impact on the electrical potential distributions along the nerve trajectories, which directly has an impact on the current levels of the stimulation. Also, it has been shown that the target nerve branches have different termination points and follow different angles based on available literature [8, 9]. Thus, analyzing the effect of nerve bending and nerve termination may guide optimizing the neuromodulator design. Investigation of such parameters may not be possible using the experimental test. It may require massive trail studies which result in costly expenses. Alternatively, the computational models are growingly used in neuromodulation therapy systems to provide important insights into the design, operation, and clinical application [10]. Such models are usually implemented in finite element (FE) models (FEM) involving a volume conductor model representing various anatomical structures, a nerve fiber model, and the electrodes by their respective conductivities and appropriate boundary conditions.

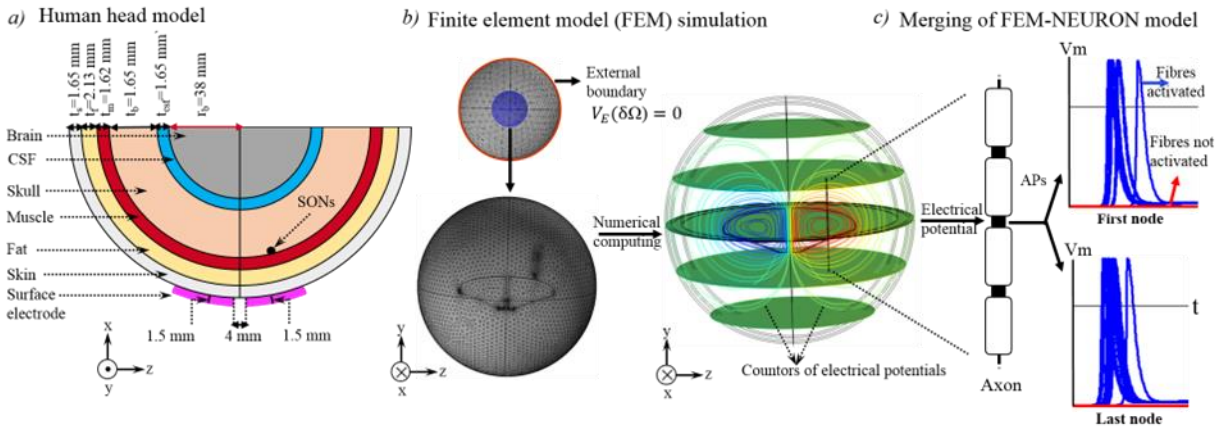

Figure 1. (a) The geometrical human head. Each layer was developed based on average thickness, r_b indicates the radius of the brain. (b.) Volume conductor of the geometrical human head model. The electrical potential distributions based on contours are highlighted. (c) Hybrid model (coupling FEM and neuron models). The extracellular potentials are applied to evaluate the response of the nerve fibers. A sample set of responses (action potentials (AP)) are shown for both the first and last nodes of the nerve fiber trajectory.

In the previous study [11], the realistic human head model was developed based on magnetic resonance imaging (MRI) and the human head was developed based on geometric shapes by mimicking the realistic human head model. It was shown that the geometrical human head could be instead with some error (3%, based on stimulus current thresholds). Also, it was shown that there is no serious effect of the microscopic structures on the stimulus current thresholds [12]. Therefore, in this study, the geometrically realistic human head (as shown in Figure 1a.) is used to evaluate the effect of nerve termination and nerve bending on the stimulus current thresholds for the target neuromodulator.

In this study, twenty different nerve models were generated to analyze the impact of nerve bending and termination on the stimulus current thresholds for given electrode settings. Each model was simulated, and the obtained extracellular potentials were distributed along the nerve trajectory to calculate nerve response to various current levels. Each model was simulated, and the obtained extracellular potentials were distributed along the nerve trajectory to calculate nerve response to various current levels.

2. Materials and Methods

2.1. Volume Conductor Model

TENS human head computational models can be constructed in a range in complexity from concentric sphere models to high-resolution models based on an individual's image data set, depending on the clinical question [13]. The anatomically specific image-based head modeling may require extensive prior work on computational modeling. In the studies [11, 12], it was shown that the geometrical human head (e.g., sphere) could be used instead of MRI a highly detailed human head model, to analyze the effect of model complexity on the stimulus current thresholds and current density with less computation cost but sufficient accuracy. As the clinical question of this study is the same (current thresholds), human head tissue layers and Cefaly patch electrodes were constructed from geometric shapes in COMSOL Multiphysics v5.2a (COMSOL, Ltd., Cambridge, U.K.). The head model consisted of six concentric spheres representing skin, subcutaneous tissue, muscle, skull, Cerebrospinal fluid (CSF), and brain, as detailed in Figure 1(a). The average thickness of each tissue

layer (skin: 1.65 mm [14, 15], fat: 2.13 mm, muscle: 1.62 mm [16], skull: 6.35 mm [17], and CSF: 1.5 mm) was used based on available literature to construct the layers in the geometrical model as indicated in Figure 1(a). As the electrical potential field decays considerably within the skull, the white and gray matter were merged and modeled as a homogeneous volume representing the brain. For this reason, the variations in the trajectory of the were only considered within the skull to the subcutaneous plane level.

It was assumed that the human head is symmetrical. Therefore, the nerve models were generated only for the left side, as shown in Figure 2. The electrode model was generated separately and merged with the skin. The full list of anatomical tissue layers, electrode patch, and their relative size are shown in Figure 1.

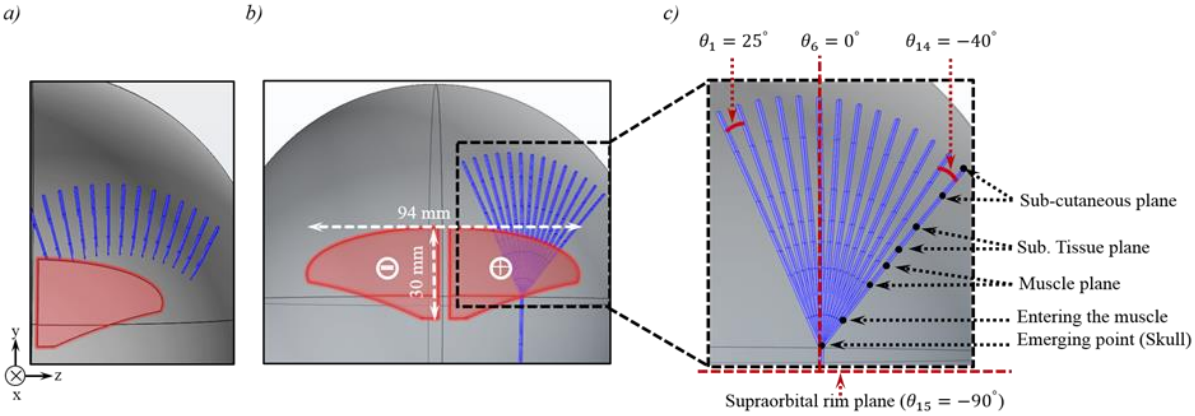

Figure 2. (a) Shows nerve trajectories on the subcutaneous plane. The nerve models are shown in blue, and the electrode patch is shown in red (b) Shows all feasible nerve models based on the statistical variation. The electrode size is highlighted. (c) Shows the generated nerve models in detail. The bending angle and the nerve transition points through the anatomical layers are labelled.

2.2. Nerve Model

The volume conductor of each nerve was constructed from geometric shapes based on the average distribution of anatomical data of SON [18, 19] using fundamental functions (e.g., *Sweep* function) in COMSOL. The SON nerve initially travels from the skull through the muscle plane and generally divides into branches as it runs in this plane. These branches enter the subcutaneous plane with different variations providing sensation to the forehead, as shown in Figure 2(c) [18, 19]. The processes of nerve modeling for nerve bending and nerve termination are detailed in the following subsections, respectively.

2.2.1. Nerve Bending

The nerve-bending models were generated based on their anatomical distributions over the forehead area. They are generated based on an incremental step, as shown in Figure 2(c). It was assured that each nerve model has the same amount of trajectory on each anatomical layer to measure the impact of the nerve bending on the stimulus current thresholds. Since there is no significant variation in the electrical potential variation from the skull layers to through the inner layers (such as the brain), the nerve models were considered from the skull layers to the superficial layers. These resulted in fourteen models in the z-direction based on assumptions. Each model was generated individually and simulated in COMSOL according to the given neuromodulator settings to simulate electrical potential variations across the nerve trajectory. The stimulus current threshold was recorded in NEURON based on a calculated electrical potential variation on each nerve model.

2.2.2. Nerve Termination

It was recorded that the electrical potential variation decays significantly after a certain distance from the superficial layers toward the inner layers. Thus, the start point of the nerve modeling was assumed to be at the skull layer boundary, as shown in Figure 3. Since the electrical parameters of the anatomical layers vary considerably (as shown in Table 1), the nerve termination point was selected by considering the enter and exit points of the anatomical layers.

It was assumed that the nerve trajectories are modeled based on the same distance from the centerline of the head to obtain a fair comparison. It is noted that the same head model was used to measure the impact of the nerve termination on the stimulus current thresholds for the given electrode and neuromodulator settings.

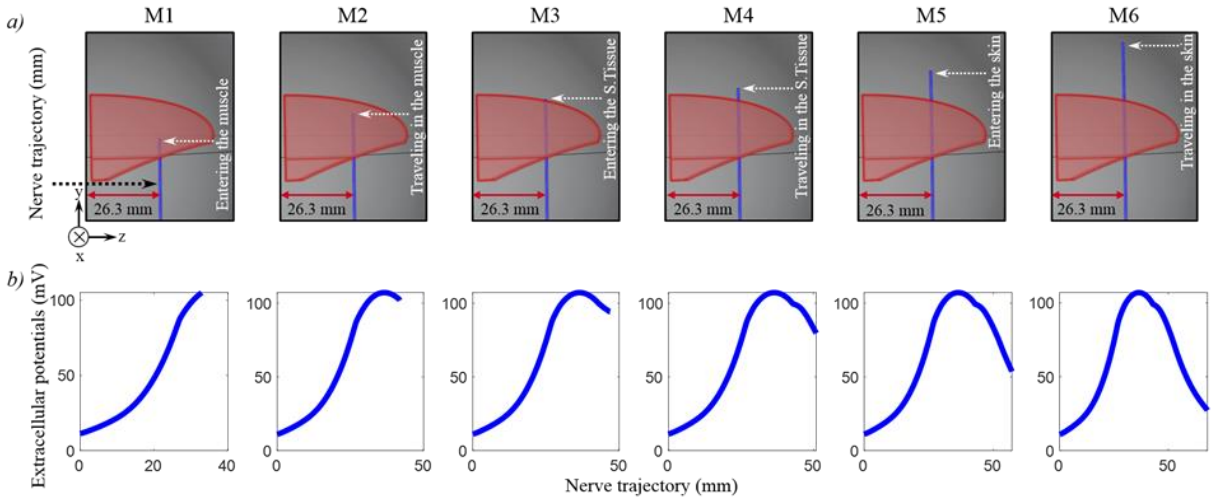

Figure 3. (a) Shows nerve termination models from Model 1(M1) to M6. The average distance of the nerve from the centerline of the forehead is shown. The nerve transition points in the anatomical layers are highlighted. (b) Shows the calculated extracellular electrical potentials along the nerve trajectories.

2.3. Finite Element Method (FEM) Based on the TENS Model

Each completed head model was simulated by dividing the geometry between the model into a mesh of small elements and solving the underlying equation for each element separately but in relation to each other in the COMSOL Multiphysics modeling environment using Cefaly electrode configuration settings.

To determine the distributions of the electrical potentials within the SON nerve in response to various stimulus strategies, the 3D finite element method was used as it provides a unique opportunity to discretize the associated domains in different element sizes during the meshing process, which is the more optimized approach to calculate electric fields in biological tissues.

2.3.1. Applying Boundary Conditions and Discretization Process

A sphere was defined around the model to implement an approximation of ground at infinity by applying the Dirichlet boundary condition (V_∞=0). To obtain the optimum sphere layer, the radius of this layer was parametrized from 150 mm to 500 mm with 50 mm incremental steps, and the electrical potential along the trajectory of the nerve was recorded for each case. There was only 1% difference in the potential value for radius from 250 mm to 500 mm. Thus, the sphere layer was generated based on 250 mm to save computation time. The domains in the volume conductor were discretized using tetrahedral meshing, while the electrode and nerve model were more finely meshed by adjusting the element size parameters. Specifically, the minimum element size for nerve and electrode domains was selected as 1 μm, and the maximum element size was set to 1 mm. The outermost layer was discretized based on the *Normal* default element size in the available software. This resulted in 3.3 M elements (about 4.1 M degrees of freedom). The average tetrahedral mesh quality and average growth rate were 6.82 and 1.3, respectively.

2.3.2. Computational Simulation

Each volume conductor of the nerve model was simulated based on a quasi-static approximation of Maxwell's equations by considering the tissues to be purely resistive. Thus, the free charge source (Q) and any external current density (J_e) in the domain are assumed to be zero. By applying this condition (Q=0, J_e=0) to equations (2) and (3), Laplace equation (4) is obtained to calculate the electric potential distribution within each FEM domain.

$$E = \nabla V \tag{1}$$

$$J = \sigma E + J_e \tag{2}$$

$$\nabla \cdot J = \nabla \cdot (\sigma \nabla V + J_e) = Q \tag{3}$$

$$\nabla \cdot (\sigma \nabla V) = 0 \tag{4}$$

where diverse operator represents with ∇, the conductivity of the tissue layers is σ, the current density and the electrical field are J and E, respectively.

An electrical current (1 mA) was applied to the anode, and the same current level was injected into the cathode. Anode and cathode electrodes were defined as Terminals in COMSOL. Thus, +1 mA was inserted in Terminal 1, and -1 mA was inserted in Terminal 2. The electrode-tissue

interface contact impedance was not considered, and appropriate continuity conditions were implemented at the boundary of each domain to obtain a unique solution [20].

A non-conductive (σ=1e^{-10} S/m) air layer was defined around the model to obtain accurate results. It is noted that the electrical parameters of each layer were defined based on the low frequencies.

2.3.3. Charge Density

Electrical stimulation may lead to tissue damage either by the flow of current across tissues or by irreversible electrochemical reactions. Thus, following safety criteria to prevent tissue damage and electrode corrosion is essential. Therefore, the charge–balanced biphasic waveform is widely used to avoid damage to electrodes and surrounding tissue. However, in addition to charge balance, the current and charge densities of the stimulation waveforms must be limited to allow charge injection by reversible processes [21, 22]. The safety limits are decided based on the charge density using Shannon safety criteria, as shown in equation (5) for electrical stimulation [23].

$$Q = IT = (A \cdot 10^{k})^{0.5} \quad (5)$$

where I is current amplitude, T is the duration of each phase (250μs) of biphasic neuromodulator pulse, A is surface area, and k is a parameter with an empirical value of 1.0–2.0. For the conservative estimation, k=1 is used. It is noted that the amount of charge per phase in each pulse is important for far-field stimulation (e.g., TENS) rather than charge density [23]. Thus, in this study, the charge density per area per phase on the electrode and along the trajectory of the average SON nerves were calculated for the neuromodulator current range.

2.4. Nerve Fiber Compartmental Model

The nerve fiver was designed based on the cable model of the mammalian McIntyre–Richardson–Grill (MRG) axon model [24]. Each nerve fiber was constructed from multiple compartments representing the nodes of Ranvier, myelin attachment segments, paranodal, and internodal sections. This simple geometric relationship remains valid for the compartments in all models. Also, the same membrane dynamics (i.e., the number of ion channels implemented) were applied in all models.

It is not clear whether fibers convey the sensation over the whole fascicle or only within a limited area, and they have different diameters. To consider these issues, Aβ fibers were designed based on their anatomical statistical distribution (whose diameters followed a Gaussian distribution with a mean of μ_D = 12.5 μm and standard deviation of σ_D = 2 μm) [7]. The associated parameters were derived by interpolating experimental measurements [24].

2.5. Merging of FEM-NEURON Model

The electrical potentials along the nerve were simulated in COMSOL, interpolated in MATLAB, and distributed along with the fibers' compartments in NEURON V7.4 to evaluate the response of nerve fibers to different amplitudes of currents. 25 μs time steps backward Euler integration was used in all simulations. All threshold values were obtained for 60 Hz and 250 μs current pulses. The percentage of activation of the nerve (PAs) for the initial and last segment of nodes was calculated for different current amplitudes. It is noted that the nerve fiber is activated when activation potentials were observed in both.

3. Results

3.1. Effects of Nerve Bending on the Current Thresholds

The extracellular potential variation along each nerve trajectory and PAs is shown in Figure 4. The results for extracellular potential variation versus the nerve trajectories for models on the left side of the forehead are shown in Figure 4(a), and the PAs of these models are shown in Figure 4(c). The results for extracellular potential variation versus the nerve trajectories for models on the right side of the forehead are shown in Figure 4(b), and the PAs versus the required stimulus current level are shown in Figure 4(d).

Figure 4(a) shows sharp variations at the bending point in extracellular potentials across all the nerve models apart from the average nerve model. It has been shown that these variations may lead to nerve activation with relatively lower stimulus current levels [25, 26]. Figure 4(b) clearly shows that the incremental variations in the bending angle lead to relatively lower stimulus current thresholds. Moreover, the more insufficient stimulus current levels are required after a certain angle (θ_2=20̊) when compared to the average nerve model (θ_6=0̊). This shows the nerve fiber can be activated with a certain level of a sharp change in extracellular potential.

Figure 4(c) indicates relatively lower variations at the bending points in the extracellular potentials for all nerves compared to models θ_1 to θ_5. Importantly, Figure 4(d) shows that all nerve models require higher current thresholds to activate the same amount of nerve fiber compared to the average nerve model current threshold. After a certain angle (θ_8=-10̊), relatively lower current thresholds are required when the bending angle is increased (with respect to the orbital rim). Interestingly, the last nerve model (θ_{14}=40̊)

stimulus current threshold is nearly identical to the average nerve model.

It is noted that the current levels are within the current range of the neuromodulator for all different angled average nerve models.

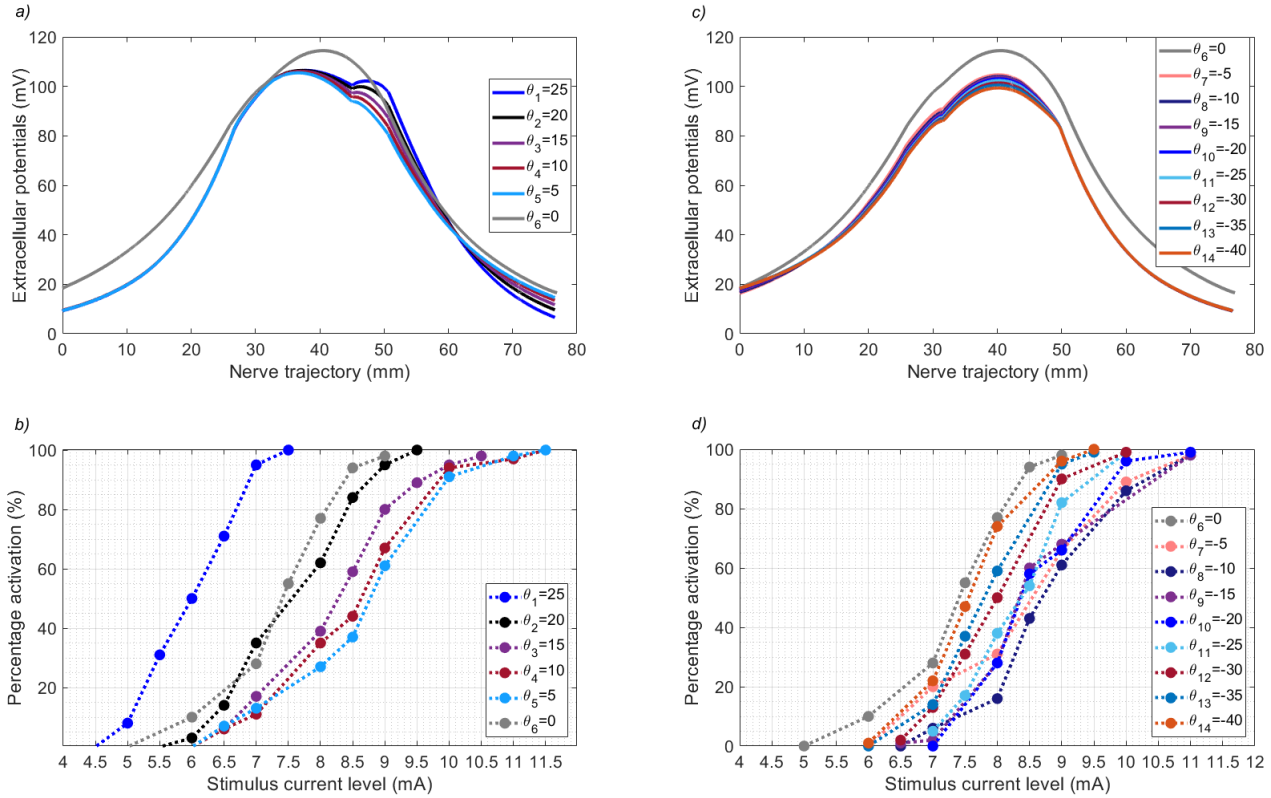

Figure 4. (a) Shows the electrical potential variation on the generated nerve bending models in the -z-direction. (b) Shows the required current levels of the nerve bending models based on the percentage activations (PAs) of the nerve fibers. (c) Shows the electrical potential variation on the generated nerve bending models in the +z direction. (d) Shows the required stimulus current levels of the nerve bending models based on the PAs of the nerve fibers in the +z direction.

3.2. Effects of Nerve Termination on the Current Thresholds

The required stimulus current levels versus PAs of the nerve fibers for the nerve termination models are shown in Figure 5.

It is noted that there is a significant effect of the nerve termination on the nerve e activation thresholds. The required stimulation current level can be reduced from 7.5 mA to around 2 mA to activate 50% nerve fiber when compared to the average nerve stimulus current threshold. Relatively more sudden changes in the electrical potentials can be observed in model 5 (M5), which leads to lower stimulus current levels. Thus, if the results in Figure 5 compare to the extracellular potential distributions in Figure 3(a), these relative stimulus current levels can be associated with the second derivative of the potentials along the nerve fiber as sharp changes resulted in lower stimulus current thresholds as also studied in [26].

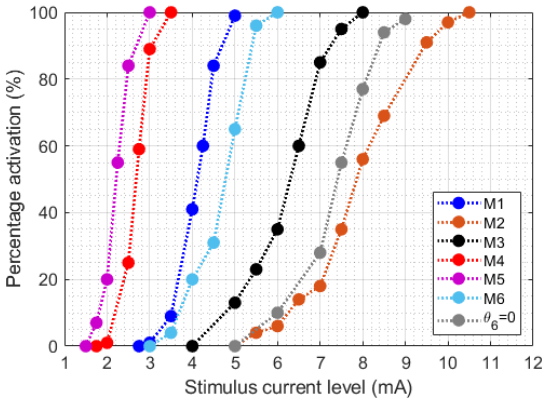

Figure 5. Shows the required stimulus current levels of the nerve fibers based on the PAs for generated nerve termination models. The result for each model is highlighted in different colors.

3.3. Estimating the Safety Limit for the Neuromodulator

The distributions of the charge density based on per

area per phase along the nerve fiber and electrode for the target neuromodulator current range are shown in Figure 6. The results of the figure are significant in safety considerations regarding the neuromodulator.

As is expected, when the current levels are increased, the charge density for both electrode and neural tissue is increased. Also, it is clearly shown that densities at the edges of the electrode are relatively higher. As the surface between two electrodes is a non-conductive medium, the charge density on this is equal to zero, as shown in the first subplot. As previously proposed, the charge density limit for large electrodes has ranged from 15 to 65 μC/cm^2/phase [23]. The result shows that the charge density for the electrode of the neuromodulator is within this range.

There is fluctuation in the nerve charge density along the nerve trajectory for all current levels due to traveling through different anatomical layers. As the nerve trajectory travels far from the electrode regarding emerging and termination points, the nerve charge density is considerably reduced in both points. The amount of charge per area per phase along the neural tissue is on the safe side of the limit for a safe charge injection [22].

The charge per area per phase density is far away compared to the safe limit for tissue damage.

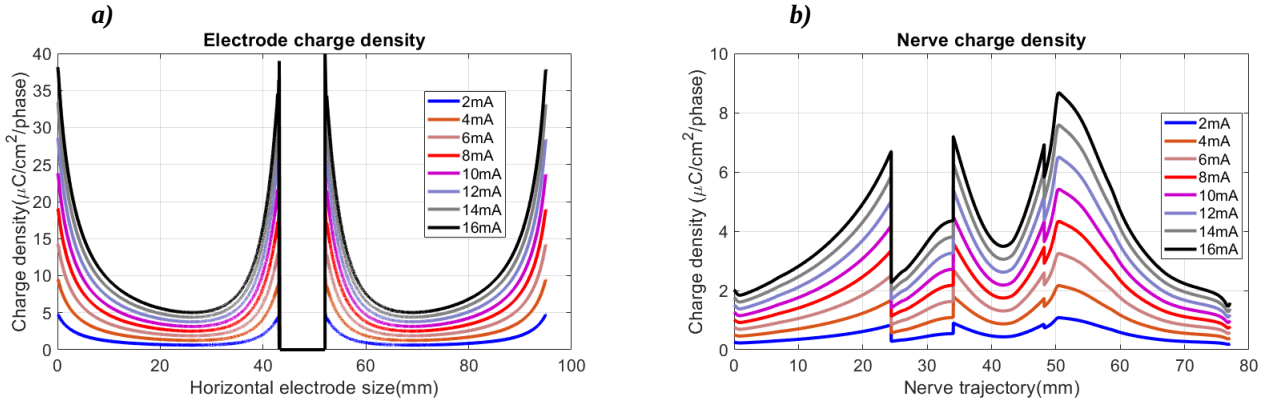

Figure 6. (a) Charge per area per phase along the electrode for a 250 μs pulse of different amplitudes using Cefaly electrode configuration. The current density is considerably higher at the edges of the electrode. The current density between the two electrode zero is due to a conductive layer. (b) Charge per area per phase along the average SON nerve for a 250 μs pulse of different amplitudes of the neuromodulator.

4. Discussing

The development of neuromodulator therapy systems for neurological disorders has accelerated with improved technologies and an expanding understanding of the effect of electrical stimulation on neural tissue. Computational methods are widely used for advancing and optimizing electrode design, stimulation parameters, and understanding the mechanism of action of these neuromodulator devices [27, 28, 29]. The TES neuromodulator procedures have been applied globally [36, 37].

It is known that the nerve termination and nerve bending angle have an impact on the nerve fiber stimulation current levels. The nerve bending point and nerve termination may lead to relatively lower required current thresholds [8, 9]. This study analyzed the effect of the nerve bending and nerve termination on the required stimulus current levels for a neuromodulator using computational hybrid FEM models. It is clearly known that the STN and SON are divided into sub-branches and these branches may terminate and bend with various trajectories and bending points. In this study, the nerve models are constructed based on the SON anatomical statistical distributions as they travel from the skull through the subcutaneous plane through the subcutaneous plane. The human head models were completed with the fundamental layers using their average statistical anatomical data distributions. Each model was simulated, and the obtained electrical potentials along the neural tissue distributed the compartments of the nerve fibers to calculate the response of different amplitudes to this field. The PAs and the activation current levels of each nerve model were recorded using the neuromodulator parameters (biphasic charge-balanced rectangular 250 μs pulses at 60 Hz) [4]. Also, the charge per area per phase was calculated to examine the safety limit for both electrode and neural tissue using the same neuromodulator parameters.

It was shown that the geometrical features of the neuroanatomical layers (e.g. nerve bending and nerve termination) have a substantial impact on the neuromodulator' current thresholds. The required current level was reduced by about 25 % based on the 50% of nerve fiber activation, comparing the furthest and average nerve models.

Also, the current study's findings suggested that the nerve angle significantly impacts the extracellular potential

distributions. Since the nerve trajectories follow different paths from the subcutaneous through the superficial plane, thus, this can be associated with the second derivative variations of the electrical potentials along the nerve fibers on the neural activation thresholds [25, 26]. It was shown that the required current levels relatively increased for the nerve models that are placed away from the center of the forehead. This can be correlated with the electrode size and shape. It is expected that the induced electrical potential variation in the vicinity of the electrode path is relatively higher. Thus, the electrical potential variations at the bending points are relatively smaller compared to the models towards the midline of the forehead, as shown in Figure 4(a), (c).

The results based on the nerve termination showed that the required current levels were relatively smaller for the nerve models that are closer to the electrode (i.e., M1 and M3) and the models that have superficial trajectories (i.e., M4 and M5). Although M2 is terminated roughly beneath the center of the electrode, the required current levels are comparatively higher. This may be related to the electrical potential variations, as the second derivative is zero at the termination point.

It is noted that the charge density per area per phase was relatively higher at the edge of the electrode due to the equipotential surface of the electrodes but was within the safe zone. The electrode edge effect happens at the metallic surface, which has an interface with the neuromodulator but not the surface that is in immediate contact with the surface of the skin on its other side. Although the charge density per area per phase for neural tissue fluctuated for various current levels, the amount of the charge per phase was far from the neural tissue damage limit.

The effect of nerve bending and nerve termination was investigated based on the average human head model. However, it has been shown that the anatomical layers in the human head have different thicknesses for each individual. Thus, the results may be affected when various human heads are considered. Another limitation of this study is the variations of the STN nerve were not considered.

Overall, the results show that the nerve bending models, which are towards the midline of the forehead, led to lower stimulus current levels after a certain bending angle, while the other resulted in higher current levels. The distance between the termination points and electrode and the superficiality of the nerve trajectory has a serious impact on the nerve trajectory have a serious impact on the nerve termination current thresholds. In most cases, the nerve bending and nerve termination led to different electrical potentials along the nerve fiber, which may result in lower stimulus current thresholds being required and this can be associated with the second derivative of these potentials variations on the activation of the neural tissue.

It noted that only a size of an electrode was considered in the current study. Using different shapes and sizes of the electrodes and targeting different nerves may provide a more insightful outcome. Thus, modeling such parameters may produce more accurate results and detailed conclusions.

5. Conclusion

The FEM models can be used to design and develop neuromodulator settings of the TES therapy systems. This study investigated the effect of nerve termination and nerve bending on the required stimulus current levels for a TES-based neuromodulator using highly realistic human head and mammalian nerve fiber models. The electrical potential along the nerve trajectories was calculated using appropriate boundary and electrical settings.

Results suggest that both nerve bending and nerve termination have a significant effect on the stimulus current thresholds of the neuromodulator, which provides critical guidance for future modeling studies and electrical stimulation design. It was shown that the nerve bending and nerve termination caused non-uniform electrical distributions, and this resulted in lower stimulus current thresholds.

Declaration of Ethical Standards

The author of this article declares that the materials and methods used in this study do not require ethical committee permission and/or legal-special permission.

Conflict of Interest

The author declares that he has no known competing financial interests or personal relationships that could have appeared to influence the work reported in this paper.

References

[1] Johnson M. I. and Bjordal J. M., 2011. Transcutaneous electrical nerve stimulation for the management of painful conditions: focus on neuropathic pain, Expert Rev. Neurother., **11**(5), pp. 735–753.

[2] Headache Classification Committee of the International Headache Society (IHS)., 2013. The International Classification of Headache Disorders, 3rd edition (beta version), Cephalalgia, **33**(9), pp. 629–808.

[3] Magis D. *et al.*, 2016. Cerebral metabolism before and after external trigeminal nerve stimulation in episodic migraine, Cephalalgia, **37**(9), pp. 1–11.

[4] Riederer F., Penning S., and Schoenen J., 2015. Transcutaneous Supraorbital Nerve Stimulation (t-SNS) with the Cefaly(®) Device for Migraine Prevention: A Review of the Available Data, Pain Therapy., **4**(2), pp. 135–147.

[5] Magis D., Sava S., d'Elia T. S., Baschi R., and Schoenen J., 2013. Safety and patients' satisfaction of transcutaneous supraorbital neurostimulation (tSNS) with the Cefaly® device in headache treatment: a survey of 2,313 headache sufferers in the general population, J. Headache Pain, **14**, p. 95.

[6] Schoenen J. et al., 2013. Migraine prevention with a supraorbital transcutaneous stimulator: A randomized controlled trial, Neurology, **80**(8), pp. 697–704.

[7] Salkim E., Shiraz A. N., and Demosthenous A., 2017. Effect of Nerve Variations on the Stimulus Current Level in a Wearable Neuromodulator for Migraine: A Modeling Study, in 8th International IEEE EMBS Conference on Neural Engineering, pp. 239–242.

[8] Schiefer M. A. and Grill W. M., 2006. Sites of Neuronal Excitation by Epiretinal Electrical Stimulation, **14**(1), pp. 5–13.

[9] Rubinstein J. T. and Rubinstein J. T., 1193. Axon Termination Conditions for Electrical Stimulation, IEEE Trans. Biomed. Eng., **40**(7), pp. 654–663.

[10] Butson C. R., Computational Models of Neuromodulation, 2012. 1st ed., **107**. Elsevier Inc.

[11] Salkim E., Shiraz A. N., and Demosthenous A., 2017. Effect of Model Complexity on Fiber Activation Estimates in a Wearable Neuromodulator for Migraine, in 2017 IEEE Biomedical Circuits and Systems Conference, pp. 1–4.

[12] Salkim E., Shiraz A., and Demosthenous A., 2018. Influence of cellular structures of skin on fiber activation thresholds and computation cost influence of cellular structures of skin on fiber activation thresholds and computation cost, Biomed. Phys. Eng. Express, **5**(1), p. 015015.

[13] Bikson M., Rahman A., and Datta A., 2012. Computational Models of Transcranial Direct Current Stimulation, Clin. EEG Neurosci., **43**(3), pp. 176–183.

[14] Takema Y., Yorimoto Y., Kawai M., and Imokawa G., 1994. Age-related changes in the elastic properties and thickness of human facial skin, Br. J. Dermatol., **131**(5), pp. 641–648.

[15] Ha R. Y., Nojima K., Adams W. P., and a Brown S., 2005. Analysis of facial skin thickness: defining the relative thickness index, Plast. Reconstr. Surg., **115**(6), pp. 1769–1773.

[16] Pinar Y., Govsa F., Ozer M. A., and Ertam I., 2016. Anatomocosmetic implication rules of the corrugator supercilii muscle for youthful eye appearance, Surg. Radiol. Anat., **38**(9), pp. 1045–1051.

[17] Ruan J. and Prasad P., 2001. The effects of skull thickness variations on human head dynamic impact responses, Stapp Car Crash J., **45**(November), pp. 395–414.

[18] Christensen K. N., Lachman N., Pawlina W., and Baum C. L., 2014. Cutaneous Depth of the Supraorbital Nerve, Dermatologic Surg., **40**(12), pp. 1342–1348.

[19] Gil Y.-C., Shin K.-J., Lee S.-H., Song W.-C., Koh K.-S., and Shin H. J., 2017. Topography of the supraorbital nerve with reference to the lacrimal caruncle: danger zone for direct browplasty, Br. J. Ophthalmol., **101**(7), pp. 940–945.

[20] Raspopovic S., Stanisa and Capogrosso, Marco and Micera, 2011. A computational model for the stimulation of rat sciatic nerve using a transverse intrafascicular multichannel electrode, IEEE Trans. Neural Syst. Rehabil. Eng., **19**(4), pp. 333–344.

[21] Cogan S. F., 2008. Neural Stimulation and Recording Electrodes, Annu. Rev. Biomed. Eng., **10**(1), pp. 275–309.

[22] Salkim E., 2019. Optimization of a Wearable Neuromodulator for Migraine Using Computational Methods, UCL (University College London).

[23] Shannon R. V, 1992. A Model of Save Levels for Electrical Stimulation, IEEE T Bio-Med Eng, **39**(4), pp. 424–426.

[24] McIntyre C. C., Richardson A. G., and Grill W. M., 2002. Modeling the excitability of mammalian nerve fibers: influence of afterpotentials on the recovery cycle., J. Neurophysiol., **87**(2), pp. 995–1006.

[25] McNeal D. R., 1976. Analysis of a model for excitation of myelinated nerve., IEEE Trans. Biomed. Eng., **23**(4), pp. 329–337.

[26] Rattay F., 1989. Analysis of models for extracellular fiber stimulation.pdf., IEEE Trans. Biomed. Eng., **36**(7), pp. 676–682.

[27] Pelot N. A., Behrend C. E., and Grill W. M., 2019. On the parameters used in finite element modeling of compound peripheral nerves, J. Neural Eng., **16**(1).

[28] Howell B., Huynh B., and Grill W. M., 2015. Design and in vivo evaluation of more efficient and selective deep brain stimulation electrodes, J. Neural Eng., **12**(4).

[29] Lempka S. F., McIntyre C. C., Kilgore K. L., and Machado A. G., 2015. Computational Analysis of Kilohertz Frequency Spinal Cord Stimulation for Chronic Pain Management, Anesthesiology, **122**(6), pp. 1362–76.

[30] Yamamoto T. and Yamamoto Y., 1976. Electrical properties of the epidermal stratum corneum, Med. Biol. Eng., **14**(2), pp. 151–158.

[31] Gabriel C. et al., 1996. The dielectric properties of biological tissues: I. Literature survey, Phys. Med. Biol., **41**(11), pp. 2231–2249.

[32] Kuhn A., Keller T., Micera S., and Morari M., 2009. Array electrode design for transcutaneous electrical stimulation: A simulation study, Med. Eng. Phys., **31**(8), pp. 945–951.

[33] Oostendorp T. F., Delbeke J., and Stegeman D. F., 2000. The conductivity of the human skull: Results of in vivo and in vitro measurements, IEEE Trans. Biomed. Eng., **47**(11), pp. 1487–1492.

[34] Baumann S. B., Wozny D. R., Kelly S. K., and Meno F. M., 1997. The electrical conductivity of human cerebrospinal fluid at body temperature, IEEE Trans. Biomed. Eng., **44**(3), pp. 220–225.

[35] "Low Frequency (Conductivity) » IT'IS Foundation." [Online]. Available: https://itis.swiss/virtual-population/tissue-properties/database/low-frequency-conductivity/. [Accessed: 20-December-2022].

[36] Gibson W., Wand B. M., Meads C., Catley M. J., and O'Connell N. E., 2019. Transcutaneous electrical nerve stimulation (TENS) for chronic pain - an overview of Cochrane Reviews doi: 10.1002/14651858.cd011890.pub3.

[37] T Mokhtari., Ren Q., Li N., Wang F., Bi Y., and Hu L., 2020. Transcutaneous Electrical Nerve Stimulation in Relieving Neuropathic Pain: Basic Mechanisms and Clinical Applications, Current Pain and Headache Reports, **24**(4). Springer. doi: 10.1007/s11916-020-0846-1.